

Soil pore network response to freeze-thaw cycles in permafrost aggregates

Erin C. Rooney ^{a,b,*}, Vanessa L. Bailey ^b, Kaizad F. Patel ^b, Maria Dragila ^a, Anil K. Battu ^c, Alexander C. Buchko ^c, Adrian C. Gallo ^a, Jeffery Hatten ^d, Angela R. Possinger ^e, Odeta Qafoku ^c, Loren.R. Reno ^c, Michael SanClements ^f, Tamas Varga ^c, Rebecca A. Lybrand ^{a,*}

^a Dept. of Crop and Soil Science, Oregon State University, Corvallis, OR, USA

^b Earth and Biological Sciences Directorate, Pacific Northwest National Laboratory, Richland, WA, USA

^c Environmental Molecular Sciences Laboratory, Pacific Northwest National Laboratory, Richland, WA, USA

^d Dept. of Forest Engineering, Resources, and Management, Oregon State University, Corvallis, OR, USA

^e Forest Resources and Environmental Conservation, Virginia Tech, Blacksburg, VA, USA

^f National Ecological Observatory Network, Boulder, CO, USA

ARTICLE INFO

Handling Editor: Yvan Capowicz

Keywords:

Pore morphology
Pore connectivity
Freeze thaw
Microscale
Permafrost thaw
Arctic
Aggregates

ABSTRACT

Climate change in Arctic landscapes may increase freeze-thaw frequency within the active layer as well as newly thawed permafrost. Freeze-thaw is a highly disruptive process that can deform soil pores and alter the architecture of the soil pore network with varied impacts to water transport and retention, redox conditions, and microbial activity. Our objective was to investigate how freeze-thaw cycles impacted the pore network of newly thawed permafrost aggregates to improve understanding of what type of transformations can be expected from warming Arctic landscapes. We measured the impact of freeze-thaw on pore morphology, pore throat diameter distribution, and pore connectivity with X-ray computed tomography (XCT) using six permafrost aggregates with sizes of 2.5 cm^3 from a mineral soil horizon (Bw; 28–50 cm depths) in Toolik, Alaska. Freeze-thaw cycles were performed using a laboratory incubation consisting of five freeze-thaw cycles (-10°C to 20°C) over five weeks. Our findings indicated decreasing spatial connectivity of the pore network across all aggregates with higher frequencies of singly connected pores following freeze-thaw. Water-filled pores that were connected to the pore network decreased in volume while the overall connected pore volumetric fraction was not affected. Shifts in the pore throat diameter distribution were mostly observed in pore throats ranges of $100 \mu\text{m}$ or less with no corresponding changes to the pore shape factor of pore throats. Responses of the pore network to freeze-thaw varied by aggregate, suggesting that initial pore morphology may play a role in driving freeze-thaw response. Our research suggests that freeze-thaw alters the microenvironment of permafrost aggregates during the incipient stage of deformation following permafrost thaw, impacting soil properties and function in Arctic landscapes undergoing transition.

1. Introduction

Arctic ecosystems are poised to undergo heightened impacts from climate change, with air temperatures rising at twice the global average rate and 40% of existing permafrost predicted to thaw over the next 80 years (Chadburn et al., 2017; Schuur et al., 2015). Permafrost thaw and associated changes to the biogeochemical function of Arctic terrestrial systems are difficult to predict due to the unique soil processes characteristic of cold regions (Biskaborn et al., 2019; Brown and Romanovsky, 2008). Freeze-thaw, a dominant process in permafrost soils, is expected

to increase in frequency and penetration depth, reaching previously frozen soil horizons. Our understanding of how the disruptive process of freeze-thaw will transform the Arctic soil environment hinges on investigating the response of thawing permafrost to repeated freeze-thaw at multiple scales.

Freeze-thaw drives soil development processes in permafrost landscapes such as frost heave, cryoturbation, and the expression of surface morphological properties including ice wedge polygons, sorted circles, and hummocks (Mackay, 1980; Ping et al., 2015; Rempel, 2010). Cryoturbation, or the sorting and mixing of different horizons, can dictate

* Corresponding authors at: Oregon State University, Dept. of Crop and Soil Science, USA (E.C. Rooney). Dept of Land, Air, and Water Resources, University of California-Davis, Davis, CA USA (R.A. Lybrand).

E-mail address: Erin.Rooney@oregonstate.edu (E.C. Rooney).

carbon distribution and protection by redistributing material from upper horizons to deeper in the soil profile where cold permafrost temperatures decrease microbial activity and promote organic matter persistence (Ping et al., 2015; Ping et al., 2008). Freeze-thaw events also regulate surface water flow and accumulation by influencing the formation of patterned ground features and associated saturation gradients (Ping et al., 2008). Shifts in microbial community function, abundance, and composition (Blackwell et al., 2010; Soulides and Allison, 1961; Storey and Storey, 2005) as well as nitrogen and phosphorus availability (Freppaz et al., 2019; Gao et al., 2018; Song et al., 2017; Zhao et al., 2021b) have been observed following single or multiple freeze-thaw events. Freeze-thaw impacts particle reorganization at the microscale which propagates to the macro-scale, emphasizing the importance of microenvironment susceptibility and response to freezing processes. The upscaled effects of pore network evolution resulting from continued freeze-thaw is demonstrated in the structural and spatial differences of pores associated with hummocks versus interhummocks in an alpine meadow study in the Qinghai Lake watershed (Gao et al., 2021). The study reported an association between individual surface features and macropore morphology as well as response to freeze-thaw. The shifting of physical properties following freeze-thaw remains less studied in thawing permafrost soil but may reflect recent findings in non-permafrost soil such as an increase in pore deformation and heightened pore connectivity after multiple freeze-thaw cycles (Liu et al., 2021b; Ma et al., 2021; Zhao et al., 2021a). Changes to the pore network architecture can have potential ramifications for organic matter decomposition (Waring et al., 2020), oxygen availability, and water flow (Wanzek et al., 2018). Given the impacts of freeze-thaw to the micro-scale biogeochemical properties and function of permafrost, additional pore-scale investigations in permafrost soils are required to better understand the impact of freeze-thaw on soils that have undergone little to no temperature fluctuations above 0 °C in recent years. Defining the response of the soil pore network to freeze-thaw is central to predicting hydrologic and carbon distribution changes within the active layer of permafrost-affected soils as well as upscaling the impacts of these changes to surface morphologic and vegetation shifts following increased warming.

The microscale response and evolution of pore networks within thawing permafrost soils represents an important knowledge gap given our limited ability to predict how pore connectivity and pore throat size distribution will change following freeze-thaw. Applying X-ray imaging (micro-computed tomography; μ -XCT) to the study of freeze-thaw in permafrost soils provides insight into how previously frozen soils may respond at the pore-level to freeze-thaw cycles (Liu et al., 2021b, 2021a; Ma et al., 2021; Zhao et al., 2021a). The impact of changes in porosity and pore connectivity on water holding capacity were reported in a recent experiment that found increased pore sizes within the 100–500 μ m range following treatments of up to twenty freeze-thaw cycles (-10°C to 6°C) in a silty loam Mollisol from northeast China using XCT analysis (Liu et al., 2021a). Microscale responses of the pore networks in permafrost to freeze-thaw deformation require additional investigation, especially in the 20–100 μ m range where soil water holding capacity and pore connectivity may be impacted. Pore-level responses can change the saturation-pressure relationship (thus altering water retention and drainage) through collapse or expansion of pore throats within critical size ranges for water holding capacity (Liu et al., 2021a). Changes in pore connectivity, pore size, and pore throat size could impact microbial accessibility to nutrients and other compounds exerting influence over decomposition rates and organic matter persistence (Waring et al., 2020). Freeze-thaw has been reported to alter pore throat morphology (Liu et al., 2021b) with an increasing number of freeze-thaw cycles corresponding to changes in the pore throat length, pore throat count, and pore throat surface area. Exposing non-permafrost, silty loam soil cores to seven freeze-thaw cycles (-10°C to 7°C) contributed to a loss of resilience in pore response as defined by the inability of the pore network to retain its original structure and connectivity following

freeze-thaw, with lower resilience evidenced by pore expansion and increased connectivity of the pore network as measured through XCT (Ma et al., 2021). Conversely, an earlier study using XCT to assess two soil textures (silty clay loam and loamy sand) from an agricultural soil in Norway found that six freeze-thaw cycles (-15°C to 40°C) reduced macro-porosity and decreased pore specific surface area of macropores, with greater effects to aggregates with coarser soil textures (Starkloff et al., 2017). A depth-based freeze-thaw study examining the impact of fluctuations between -10°C and 20°C in an alpine permafrost meadow soil identified decreases in pore connectivity (XCT) following five freeze-thaw cycles and decreased water infiltration following ten freeze-thaw cycles within the first 7.5 cm of the soil, with a variation of freeze-thaw response of the pore network by soil depth and soil texture (Zhao et al., 2021a).

The objective of our research was to measure the impact of repeated freeze-thaw cycles on the physical structure of permafrost aggregates using non-destructive, high resolution XCT imaging capabilities at resolutions of 20 μm . Specifically, we measured how soil pore networks in macroaggregates (2.5 cm^3) subsampled from permafrost soils (Toolik, AK) responded to five experimental freeze-thaw cycles (-10°C to 20°C) that simulated conditions relevant to Arctic surface environments (NEON, 2021a). We investigated pore morphology and deformation due to freeze-thaw by measuring pore connectivity and pore throat diameter distribution before and after freeze-thaw events. We hypothesized that freeze-thaw would increase pore connectivity across all aggregates through the expansion of smaller pore throats ($<50 \mu\text{m}$), based on findings from prior work (Deprez et al., 2020; Liu et al., 2021b; Ma et al., 2021; Starkloff et al., 2017). We provide a pore-scale perspective on changes to the pore network occurring at this incipient stage of permafrost warming, specifically within the first five freeze-thaw cycles following thaw. Our work contributes to the current understanding of freeze-thaw deformation while providing data needed for future predictions of how climate warming will alter the physical properties of globally important Arctic landscapes.

2. Materials and methods

2.1. Field setting selection

The National Ecological Observatory Network (NEON) Toolik site is part of the Toolik Field Station, located at 828 m above sea level within the Arctic foothills of the Brooks Range, with tussock tundra and dwarf shrub comprising the dominant vegetation (National Ecological Observatory Network, 2019). Mean annual precipitation is 316 mm (including an average of 176 mm of precipitation as snow) with a dominant southerly wind direction, a mean annual temperature of 10.1°C , and an average snow depth of 50 cm (DeMarco et al., 2011; NEON, 2021b; Wang et al., 2012). Toolik, Alaska was an ideal study area due to its shallow active layer, minimal freeze-thaw history, and available soil temperature instrumentation. The site falls within the continuous permafrost zone with soils classified as Gelisols (NEON, 2021c; Soil Survey Staff, 1999) derived from Holocene glacial moraines and alluvial deposits (U.S. Geological Survey, 2005). Three soil cores (less than one meter in depth) were collected from the Toolik site on an east-facing slope shoulder toward the base of a plateau in April of 2016 (Fig. 1). Cores were extracted using a Giddings' probe (Giddings Machine Company, Windsor, CO, USA), and shipped frozen to Oregon State University (OSU) and preserved at -40°C .

To confirm that Toolik experiences little to no recent freeze-thaw cycling at the depths sampled (to allow us to target incipient stages of deformation following permafrost thaw), we used temperature data available for the site (NEON, 2021a) and calculated the number of freeze-thaw cycles by season between 2018 and 2020 (fall, winter, spring, summer) using the *FTCQuant R* package (Boswell et al., 2020b). For computational functionality, soil temperature data from sensor units were excluded if missing data exceeded 3% of measurement time points

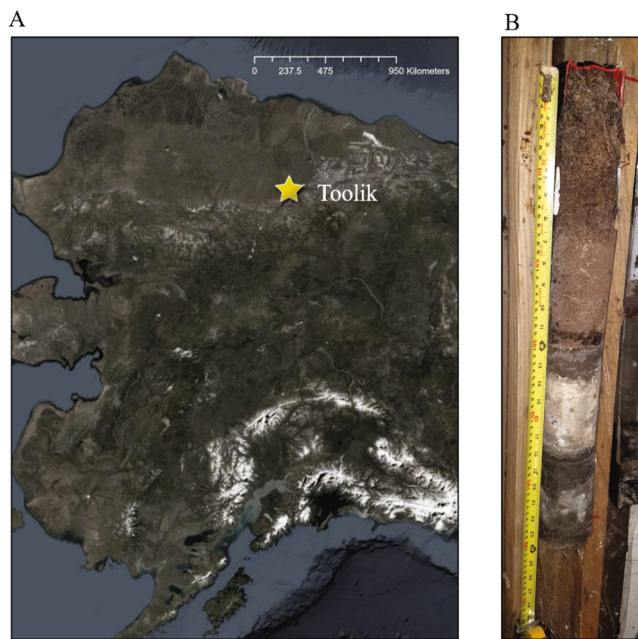


Fig. 1. (A) Map of Alaska with Toolik Field Station indicated by the yellow star. (B) 67 cm soil core collected from the NEON site at Toolik, AK and sampled for XCT analysis. (For interpretation of the references to color in this figure legend, the reader is referred to the web version of this article.)

within each analysis time frame, resulting in one to five usable time series measurements for each depth by season combination. Freeze-thaw analysis within the *FTCQuant* package uses time series temperature data to estimate the number of times soil temperature was below and above a defined temperature cutoff for more than a defined duration of time. For this analysis, we defined freeze-thaw cycles as soil temperature fluctuations persisting for a minimum of twelve hours $< -2^{\circ}\text{C}$ and a minimum of twelve hours $> 2^{\circ}\text{C}$. These parameters align with previously published freeze-thaw methods (Boswell et al., 2020a,b; Henry, 2008; Ma et al., 2021). The results from this analysis can be found in *Supplemental Fig. S1*.

2.2. Sample preparation

Cores were described morphologically according to pedological characteristics including organic and mineral material (Ping et al., 2015; Soil Survey Staff, 2014). Six aggregates (two per core) were collected from upper mineral permafrost horizons (Fig. 2). The aggregates were ~ 2.5 cm in diameter and were collected from the same morphological horizon within each core. Sampled depths targeted uniform soil texture, classified as silt loam (23.07% sand, 56.8% silt, and 20.13% clay) with $\sim 11\%$ organic carbon content (Nave et al., 2021). Core A aggregates were sampled between 28 and 38 cm, Core B aggregates sampled between 40 and 50 cm, and Core C aggregates sampled between 41 and 50 cm.

Samples were collected from each core using a chisel and mini sledgehammer to create 5–10 cm thick soil disks, allowing natural aggregates to separate as disks broke apart. Aggregates were air-dried at 20°C for 24 h and then re-wet with deionized water using a sterile dropper to moisture contents of either 12–16% or 28% weight water content. The aggregates were air-dried in order to ensure both consistent moisture content and adequate aggregate strength to avoid sample loss during freeze-thaw treatments and scanning with XCT prior to and following the freeze-thaw treatments. Once rewet to the target moisture, aggregates were fit tightly (aggregates edges were in contact with the tube walls) into 15 mL plastic conical-bottom centrifuge tubes for the remainder of the experiment to hold aggregates in a set position and identical orientation for the before and after freeze-thaw scans. The two moisture contents were selected to represent the potential for seasonal variability in soil wetness, both saturation (28%) and dry conditions (12–16%).

2.3. Freeze-thaw incubation

Each aggregate underwent five freeze thaw cycles of 20°C (thaw) to -10°C (freeze) in a temperature-controlled chamber (Refrigerator/Freezer Isotemp, Fisher Scientific) with each full cycle taking four days (two days for thaw and two days for freeze). The large range in soil temperature and duration was selected to ensure that each freeze-thaw cycle occurred fully and equally throughout the soil. Full freezing/thawing was achieved in <24 h for the amount of soil used (2.5 cm

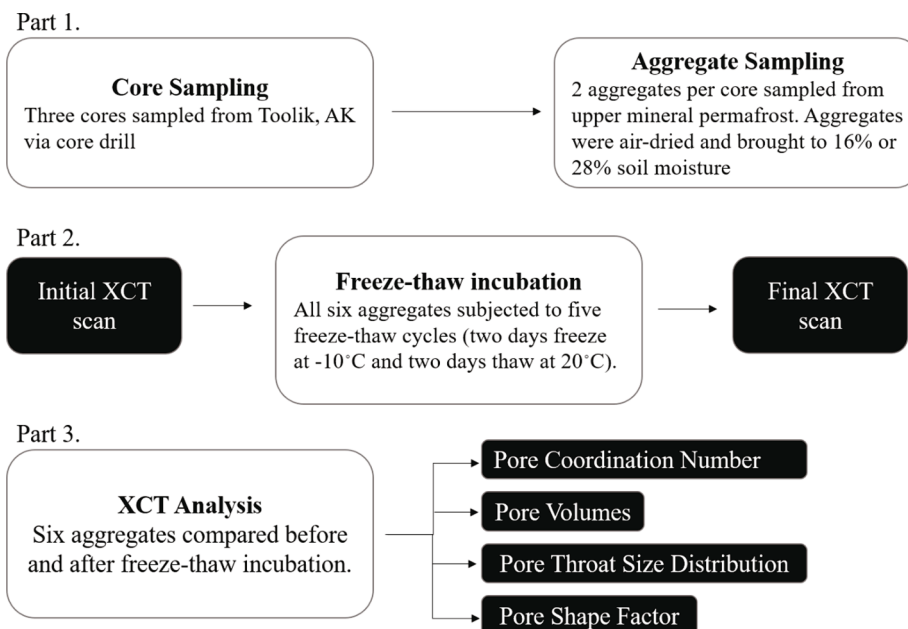


Fig. 2. Experimental Design. Three cores were sampled from Toolik, AK. Two aggregates per core were sampled from upper mineral permafrost horizons. Aggregates underwent five freeze-thaw cycles with XCT scans performed at the beginning and end of the freeze-thaw incubation.

diameter aggregate), however an extra 24 h was added to ensure completion of the freeze–thaw cycle (Ma et al., 2021). Aggregates were maintained in a closed system (Parafilm and tight-fitting lids over centrifuge tubes) to prevent moisture loss.

2.4. XCT scanning and image segmentation

Soil aggregate samples were imaged before and after the freeze–thaw incubation in plastic conical-bottom centrifuge tubes using XCT on an X-Tek/Metris XTH 320/225 kV scanner (Nikon Metrology, Belmont, CA). Data were collected at 100 kV and 400 μA X-ray power. A 0.5-mm thick Cu filter was used to enhance image contrast by blocking out low-energy X-rays. The samples were rotated continuously during the scans with momentary stops to collect each projection (shuttling mode) while minimizing ring artifacts. A total of 3000 projections were collected over 360° rotation recording 4 frames per projection with 708 ms exposure time per frame. Image voxel size was 10.2 μm . The images were reconstructed to obtain 3D datasets using CT Pro 3D (Metris XT 2.2, Nikon Metrology). Representative slice and 3D images were created using VG Studio MAX 2.1 (Volume Graphics GmbH, Heidelberg Germany) and Avizo 2019.2 (Thermo Fisher Scientific, Waltham, MA). Image processing and porosity analysis was carried out using Avizo 2019.2. The reconstructed 3D volume data was filtered using a median filter and cropped to comparable (between aggregates) rectangular prism shaped volumes of an average of $620 \times 674 \times 792$ voxels to exclude surrounding air space while maximizing the analyzed soil volume.

2.5. XCT data processing

The XCT data processing method followed a multistep protocol outlined in [Supplemental Fig. S2](#). Each image was first segmented into air, water, low-density soil, and high-density soil, based on manual thresholding ([Supplemental Figs. S3–S5](#)). Each voxel was assigned a value between 1 and 4 that correlated to its assigned component (i.e., air, water, soil, and high-density soil). Air and water voxels were then selected from the segmented image and an “OR” operation (binary operation to provide all the voxels that are water or air) was conducted to create a binary image that combined water and air. We used both the air and water voxels as the pores are connected by waterways, even if individual pores were not connected directly by air space. Following segmentation, we extracted (1) air and water-filled pore volumes from both the connected pore network and unconnected pores, (2) pore coordination numbers (defined below), and (3) pore throat diameters ([Fig. 2](#)). These data were obtained for soil pores down to a resolution of 20 μm . This minimum resolution was twice the resolution of measured voxels.

2.5.1. Pore connectivity

Determining pore connectivity required the selection of parameters that pores must adhere to in order to be considered “connected” and part of the main pore network. Using the Axis Connectivity Module in Avizo, we required pore networks to extend between two opposing faces of the volume’s bounding box. The opposing faces were defined as two planes normal to either the X, Y, or Z axis depending on which axis was most suitable to the pore network of each individual sample. In cases where no volumes satisfied the axis connectivity requirements, we defined the connected pores as the connected group of water/air with the largest volume using the Filter by Measure module in Avizo.

2.5.2. Pore coordination numbers

Coordination number represents the number of other pores to which a specific pore is connected. Coordination numbers were obtained by converting pore structure into a ball (pore node) and stick (connected paths between pore nodes) model (Li et al., 2019). The number of nodes a given node is directly connected to dictates its coordination number, i.e., a pore node connected to three other pore nodes has a coordination number of “3” ([Supplemental Fig. S6](#)). This metric provides information about the connectivity of the pore network, with before and after freeze–thaw comparisons of the distribution of coordination numbers to illuminate if and how connectivity is changing.

2.5.3. Pore throat diameter distributions

The watershed algorithm was used to separate and define individual pore regions within the pore network as distinct objects (interpretation: 3D; Neighborhood: 26; Marker Extent: 27; Output type: Split; Algorithm Mode: Repeatable) (Ferreira et al., 2018). Following delineation of individual pore regions, connected and unconnected pores and pore throats were identified using the “XOR binary operation” (to quantify the difference between all pore network voxels and distinct pore voxels) (e.g., shown in [Fig. 3](#)). Volume measurements for pore regions were extracted using the AVIZO software for unconnected and connected pore regions delineated by water and air. Pore regions were defined as the pore area that was not included in the pinch point between two pores. Pore throats are conventionally defined as the constrictive region (pinch point) between pores (Nimmo, 2013). Within an XCT context we defined pore throats as connecting regions (voxels of equivalent grey scale intensity to those of pores) between individual pores within the connected pore network. Throats were not part of the distinct individual pores but rather pinch points representing the connecting region between two neighboring pores. Each pore throat was manually given a unique label before the volume, equivalent radius, surface area, feret width, feret length, and feret breadth were calculated and then compared to a manually measured pore throat diameter to determine which metric was most representative. Feret breadth was not significantly different from manually calculated pore throat diameter (LME, $F = 3.7265$, $P = 0.1258$) and was highly correlated with the manually calculated diameters ($R^2 = 0.96$, $P = 0.01$) ([Supplemental Table S1](#), [Supplemental Fig. S7](#)). Equivalent radius was less accurate than feret breadth for the pore throat sizes we studied ([Supplemental Fig. S8](#)). Thus, we used breadth as a proxy for pore throat diameter herein.

2.5.4. Pore shape factor

Pore shape factor for pore throats was calculated as the ratio between the pore throat’s surface area and its spherical equivalent surface area, which is the surface area of a sphere with the same volume as the pore throat. Spherical pore throats contain pore shape factors between 0.75 and 1.00 versus ratios < 0.75 for more irregular or elongated pore throats < 0.75. The equation for pore shape factor:

$$SF = \frac{A_o}{A}$$

A_o represents the spherical equivalent surface area while A is the actual surface area (Wadell, 1933). The spherical equivalent surface area formula was:

$$A_o = 4\pi \left(\sqrt[3]{\frac{3}{4\pi} V} \right)^2$$

With V being the volume of the pore throat. This formula used the volume of a sphere solved in terms of the radius, $r = \sqrt[3]{\frac{3}{4\pi} V}$, and the formula for the surface area of the sphere, $A = 4\pi r^2$.

2.6. Post processing and filtering

Artifacts were identified and removed by filtering the data post-processing. Artifacts included incorrectly identified pore throats (noise) composed of less than five voxels as well as large, distinct regions of the pore network erroneously separated into two separate regions, falsely creating pore throats. Both types of artifacts were identified based on their volumes and were filtered out of the data by removing all

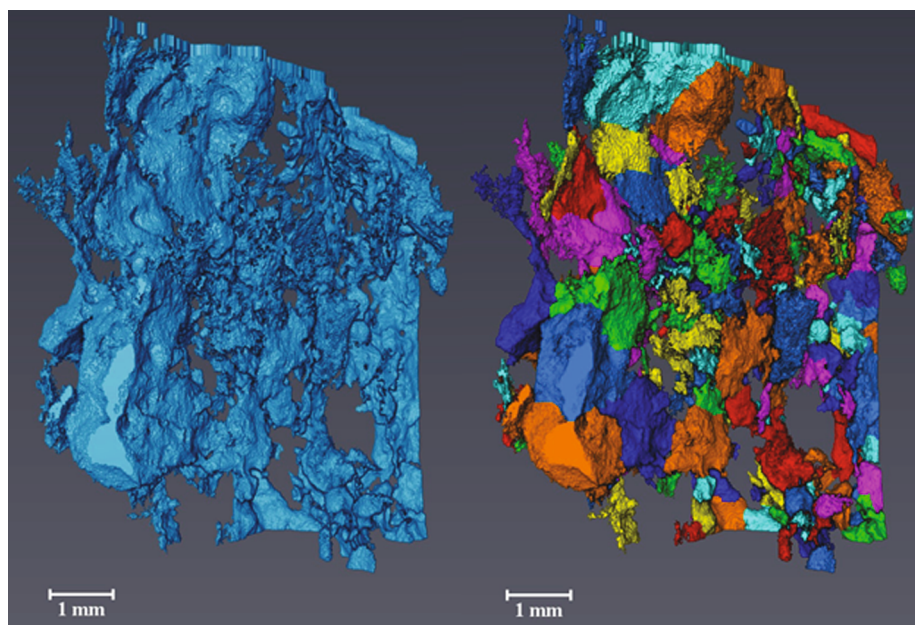


Fig. 3. Rendering of the connected pore network from Aggregate C_{28%}. Example of (left) the unseparated pore network and (right) separating objects as connected objects, representing individual pores in our analysis.

pore throats with a volume $>0.5 \text{ mm}^3$ or less than five voxels. Occasionally, pore nodes were also filtered out when errors in the pore network model created pore nodes with coordination numbers of zero. All filtering was done within Microsoft Excel prior to data analysis in R/RStudio.

2.7. Data analysis

We used linear mixed-effects models (LME) to test the effect of freeze–thaw cycles on pore volumetric fractions, pore coordination number, and pore throat count. Sample number and/or moisture content was used as a random effect. Statistical significance was determined at $\alpha = 0.05$ given the heterogeneous pore morphology and the limited number of samples available due to the time-intensive nature of the XCT analyses. All data analyses were performed in R version 4.0.1 (2020–06–06) (R Core Team, 2020), using primarily the *dplyr v1.0.1* (Wickham et al., 2020) package for data processing and analysis, and *ggplot2 v3.3.2* (Wickham, 2016) and *PNWColors* (Lawlor, 2020) packages for data visualization. All data and scripts are available at <https://github.com/Erin-Rooney/XCT-freezethaw> (<https://doi.org/10.5281/zenodo.5816355>) and archived and searchable at <https://search.emsl.pnnl.gov/>.

3. Results

3.1. Pore morphology

All six aggregates displayed soil pore networks with distinctive pore morphologies (Fig. 4), indicating a variation in physical microenvironments that was also observed in differing median pore throat diameter (LME, $F = 15.3894$, $P = 0.0047$) and mean pore throat diameter (LME, $F = 9.9005$, $P = 0.0125$) across aggregates (Supplemental Table S3). Despite variation in pore morphology across aggregates, we observed structural similarities shared between aggregates of the same core (Fig. 4). For example, both aggregates sampled from Core A at a depth of 28–38 cm contained large, irregularly shaped pore structures ranging from 0.75 to 2 mm (Fig. 4a–b). The pore morphologies of the two aggregates sampled from Core B were similar to each other while differing visibly from Core A and C aggregates. Both B_{16%} and B_{28%} contained large platy pores (reminiscent of ice-lenses) that were intersected perpendicularly by a large tubular feature (Fig. 4c–d). The two

aggregates from Core C contained several larger pore structures surrounded by many small to medium irregularly shaped pore structures (Fig. 4e–f). C_{16%} contained large tubular structures similar to those in Core B but were not seen in C_{28%}. There were also similar platy pores occurring perpendicular to the tubular channel for C_{16%}, although the pores were less prominent in comparison to the platy pores observed in the aggregates from Core B (Fig. 4e). The second aggregate, C_{28%}, had several large, connected, irregularly shaped pore structures and no tubular pores (Fig. 4f).

3.2. Pore connectivity and volumetric fractions

Connected water-filled pore volumetric fraction decreased following freeze–thaw (LME, $F = 9.19774$, $P = 0.0142$; Fig. 4). All aggregates displayed this decrease in the connected water-filled pore volume with the exception of B_{28%}. Despite decreasing volumes of connected pores there was no corresponding increase in any other volumetric fraction (e.g., connected air-filled pores, unconnected air-filled pores, unconnected water-filled pores) in any aggregate.

While we were unable to test for a statistical relationship between pore morphology and connectivity changes following freeze–thaw, there was a variation in the magnitude of changes following freeze–thaw. Subtle changes occurred in aggregates A_{16%}, B_{16%}, and B_{28%} with all pore types (air-filled, water-filled, connected and unconnected) showing low magnitude response to freeze–thaw (Fig. 4a, c, d). In contrast, C_{16%} and C_{28%} showed some of the largest reductions in the connected water-filled pore volumetric fraction, while C_{16%} demonstrated the only case of a large tubular pore structure detaching from the connected pore network following freeze–thaw (Fig. 4e–f). It is difficult to determine if the changes in pore volumetric fractions observed in A_{28%} are the result of freeze–thaw or primarily because pre and post freeze–thaw scans were made in two different regions of the same aggregate (Fig. 4b).

The variation in pore structure between the before and after scans of A_{28%} taken from different regions of the same aggregate indicated the potential for physical heterogeneity both across aggregates and within aggregates at a spatial difference of $<2.5 \text{ cm}$ (Fig. 4). Despite morphologic differences between two regions of the same aggregate, there were marked similarities in freeze–thaw response between A_{28%} and the other aggregate from Core A (A_{16%}) including the pore throat diameter and pore coordination number distributions (Figs. 5 and 6, Supplemental

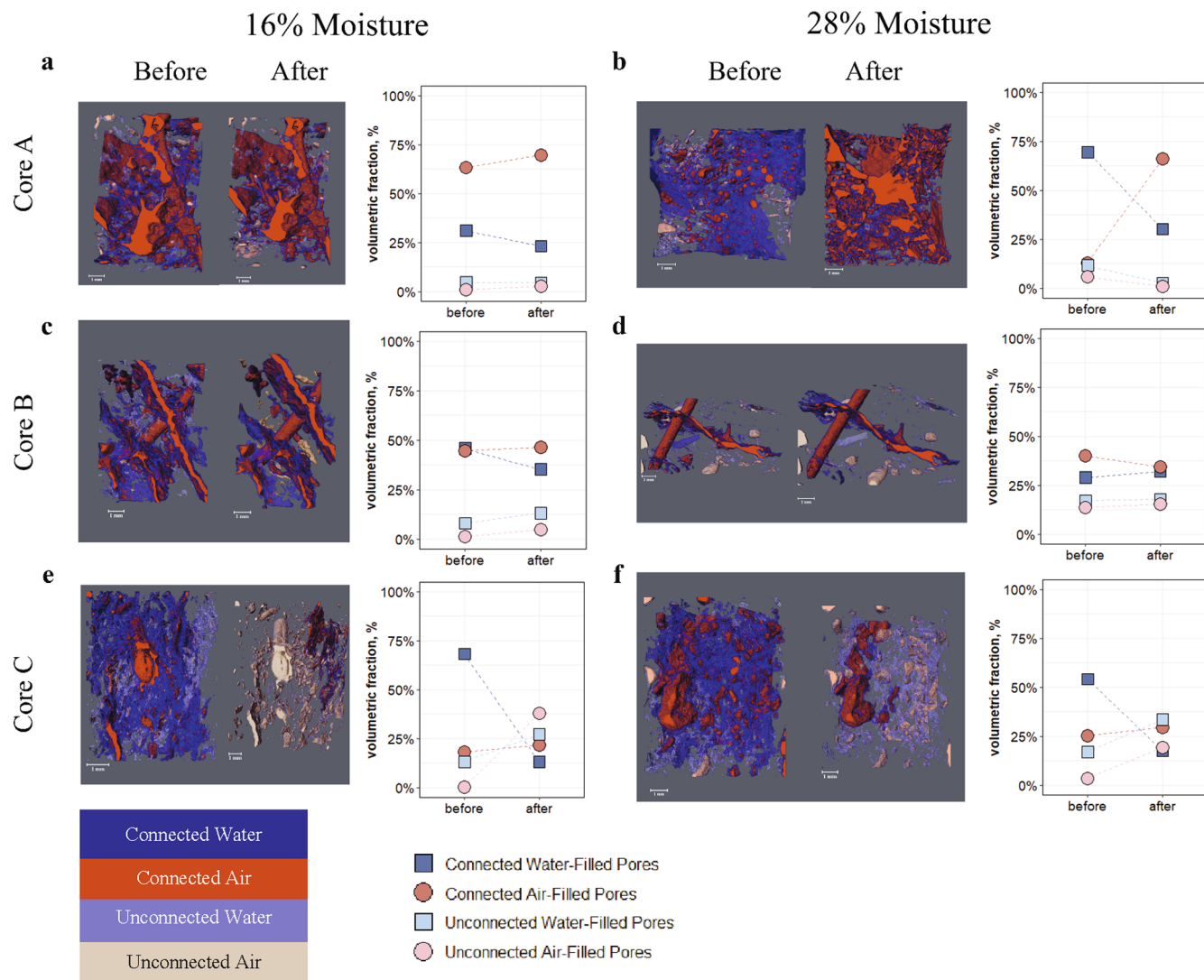


Fig. 4. XCT images of aggregates before and after freeze–thaw with connectivity and type indicated by color. Connected water-filled pores are blue, connected air-filled pores are red, unconnected water-filled pores are light blue, and unconnected-air filled pores are tan/pink. The volumetric fractions (in percent) of connected and unconnected air and water-filled pores (measured through XCT) are represented across the six experimental aggregates before and after freeze–thaw. Dashed lines provided for ease of viewing. Change in the connected water volumetric fraction was significant (LME, $F = 9.1977$, $P = 0.0142$). No changes in any other volumetric fraction were significant. (For interpretation of the references to color in this figure legend, the reader is referred to the web version of this article.)

Table S2. The differing pore morphology within the same aggregate combined with similarities in freeze–thaw response observed in the Core A aggregates is contrasted by the aggregates from Core B. The Core B aggregates, despite similar pore morphologies, displayed differences in the response outcomes of freeze–thaw (Fig. 4). $B_{16\%}$ responded to freezing and thawing in a similar fashion as the other four aggregates. In contrast, $B_{28\%}$ was the only aggregate to have an increase in the connected water-filled pore volumetric fraction (where all other aggregates showed decreases) and a decrease in the frequency of less connected pores following freeze–thaw. The effect of freeze–thaw on pore connectivity differed by pore coordination number (LME, $F = 5.8401$, $P < 0.0001$) with the greatest impact on pore coordination number 1 (Fig. 5). Before freeze–thaw, approximately 20% of pores had a pore coordination number of 1 whereas this percentage increased to 40–60% for half the aggregates following freeze–thaw (Fig. 5, [Supplemental Table S2](#)). For pore coordination numbers 2–16 we saw variable response and in the highest pore coordination numbers we saw little to no response to freeze–thaw. There was no effect of freeze–thaw on total connected pore volume, defined as the combined connected air and water volumetric fractions.

3.3. Pore throat diameter

Pore networks showed aggregate-specific responses to freeze–thaw, but with consistent patterns associated with specific pore throat diameter sizes (Fig. 6). Across all aggregates, pore throats in the 30 to 50- μm diameter range responded to freeze–thaw with both increasing and decreasing pore throat diameters, resulting in non-uniform changes to the pore throat diameter distributions within that range.

We tested pore shape factor of pore throats to identify the type of deformation (elongation or sphericalness) occurring within changing pore throat sizes. However, pore shape factor did not change significantly following freeze–thaw across any pore throat size ranges (LME, $F = 1.1556$, $P = 0.1295$, [Supplemental Fig. S9](#)). Pore throats up to 100 μm in diameter showed a difference in frequency following freeze–thaw, although the direction of change varied across all aggregates and moisture contents. The frequency of pore throats over 50 μm decreased following freeze–thaw primarily in the higher moisture (28% moisture) aggregates (Fig. 6).

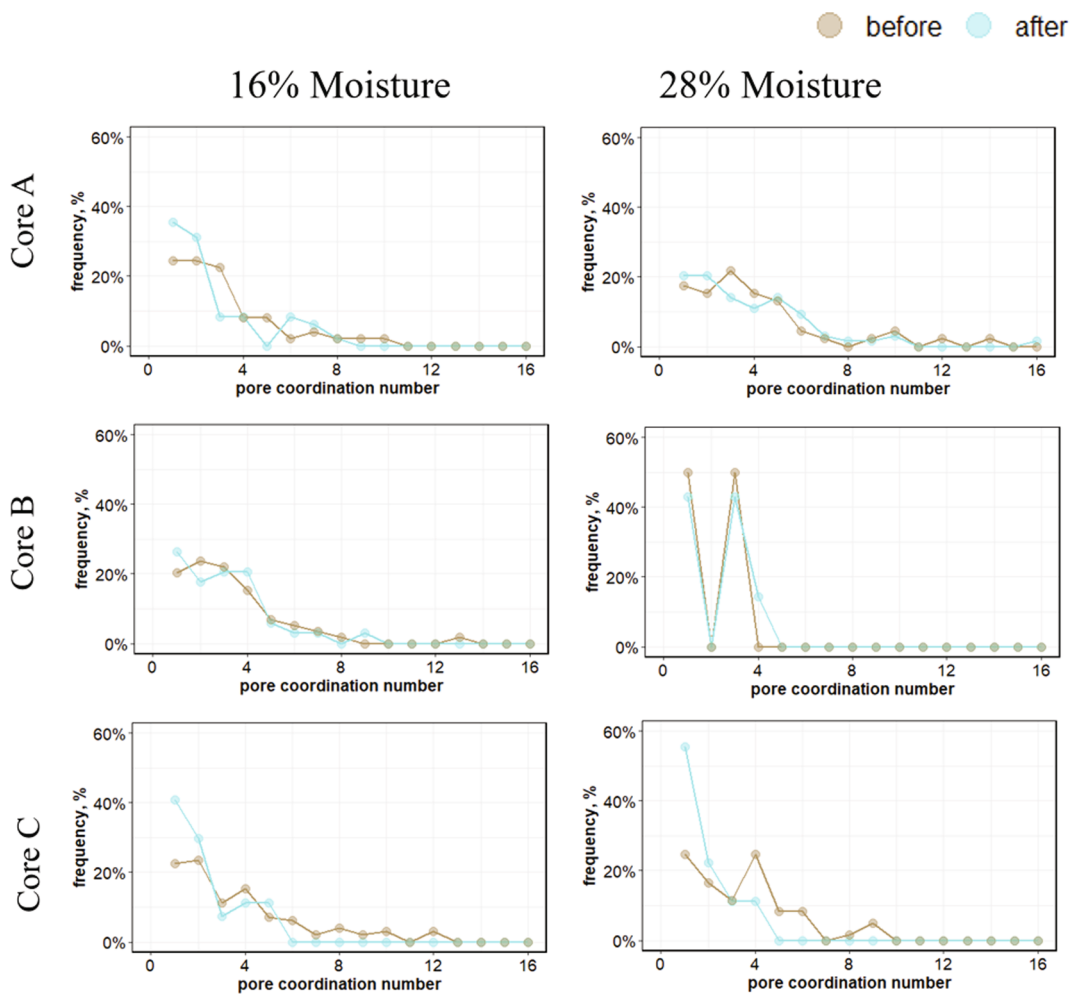


Fig. 5. Pore coordination number frequency before and after freeze–thaw. Higher frequencies indicate an increase in the occurrence of a pore coordination number. Frequency was calculated as the count/total count. The effect of freeze/thaw differed by pore coordination number (LME, $F = 5.84007$, $P < 0.0001$).

4. Discussion

4.1. Pore morphology

The complex relationship between initial pore morphology and pore network response to freeze–thaw highlights the potential for heterogeneity of microbial habitats within thawing permafrost soils (Bailey et al., 2013; Wanzenk et al., 2018; Waring et al., 2020). Water flow and subsequent nutrient diffusion and redox conditions have been correlated with pore connectivity (Wanzenk et al., 2018). Pore size and structure have also been posited to play a role in organic matter persistence or decomposition, with a recent model simulation (PROMISE) suggesting greater potential for microbial-facilitated chemical transformations in the “flow-permitting pore size class” of macropores over 1 μm in size (Waring et al., 2020). The variability in freeze–thaw response of the individual pore architecture of each aggregate and the potential dependence on initial pore morphology indicates a complexity in structural changes of the pore environment under freeze–thaw action, with implications for predictive modeling of water flow, redox chemistry, and organic matter persistence.

As indicated by the pore morphologies represented within our study, we suggest that platy/lenticular pores—such as those associated with ice-lens development, (Darrow and Lieblappen, 2020; Rempel, 2010)—may result in higher variability of structural freeze–thaw-response than other types of pore morphologies observed within aggregates (e.g., large, asymmetrical pores or tubular pores surrounded by small,

spherical pores). The two aggregates from Core B with similarly platy pore structures showed heterogeneous responses in shifting pore coordination numbers and connected water-filled pore volumetric fraction changes following freeze–thaw. B_{28%} displayed decreases in the frequency of less connected pores and increases in the connected water-filled pore volumetric fraction while B_{16%} aligned more closely with changes in pore connectivity shown by aggregates from Core A and Core C. The potential for specific pore morphologies to respond in characteristic ways to freeze–thaw requires additional investigation, with implications for permafrost soils that show variable responses to freeze–thaw in terms of pore connectivity and pore throat size distribution. This pore architecture-based variability would need to be accounted for in predictions for how water, gas flow, and carbon protection could change following increased freeze–thaw in previous permafrost. For example, the high carbon content associated with deeper soil horizons with cryoturbation history (Jelinski et al., 2019; Ping et al., 2015, Ping et al., 2008) occurs at depths that are likely to undergo additional freeze–thaw action under warming (Wei et al., 2021).

The pore morphologies in both aggregates from Core B are similar to ice-lenses, that form as a result of frost heave and are prominent features within the active layers of documented permafrost soil profiles (Andersland and Ladanyi, 2004; Mackay, 1980; Rempel, 2010). The presence of these pores was unexpected since the aggregates were purposefully selected from the permafrost horizon of the soil profile. Previous research has found that isothermal frost deformation that

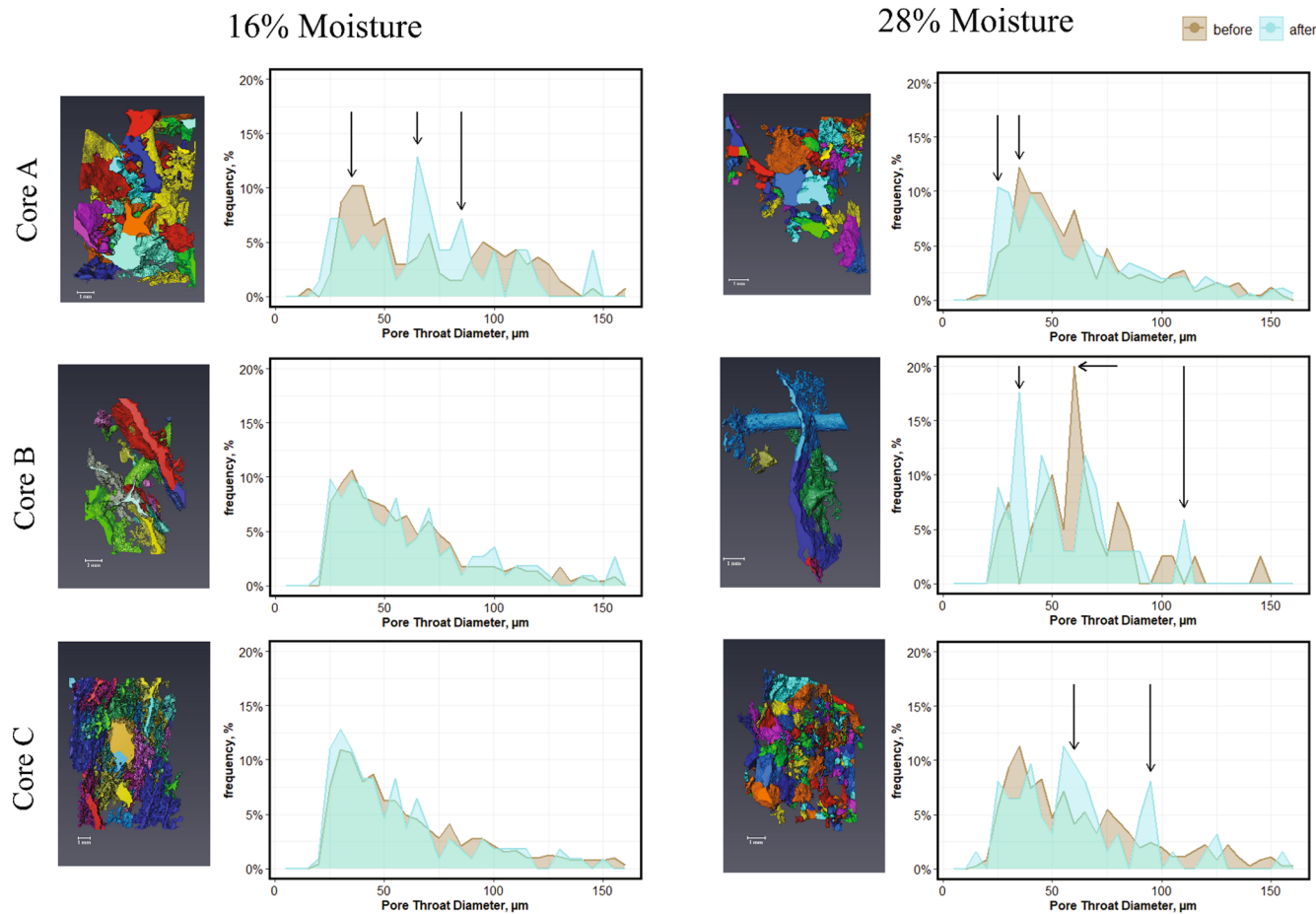


Fig. 6. Connected pore network with individual pore regions highlighted by color and pore throat diameter distribution frequencies (bin size = 5 μm) before and after freeze–thaw for each aggregate. Frequency was calculated as the count/total count. Arrows represent regions with the largest changes in frequency following freeze–thaw.

generates these features could occur at subzero temperatures due to pore-scale heterogeneities causing pressure gradients and thus seepage of water from smaller pores to larger pores (Rempel and van Alst, 2013). It is also notable that the pore morphologies from both aggregates in Core B contain a large tubular channel running perpendicular through the platy pore structures that could be formed by root penetration or frost heave. If root-caused, the tubular channel may have resulted in compressive forces that facilitated development of the ice-lens-like pore structures, offering an alternate explanation for their occurrence. However, our review of the literature shows little research conducted in this area with no identification of platy pores co-occurring with root deformation (Veelen et al., 2020), leaving this possibility in need of further examination. While aggregates from Cores A and C did not display ice-lens-like pore structures, it is possible that frost heave processes following active layer thickening and permafrost thaw could result in a higher occurrence of these pore morphologies in the future following continued freeze–thaw and subsequent frost heave (Ping et al., 2015; Rempel, 2010). A shift from pore networks consisting of high densities of smaller pores toward networks composed of larger, elongated pores following freeze–thaw is supported by recent findings which posited that these channel pores may also be partially caused by breakage along internal structural weaknesses of the aggregates exploited by freeze–thaw (Liu et al., 2021b; Ma et al., 2021).

4.2. Pore connectivity and volumetric fractions

Based on the differences in initial pore network morphology across aggregates from Cores A, B, and C, we expected to see large variability in

freeze–thaw response, with the most similar freeze–thaw responses occurring in aggregates that shared similar pore network morphologies and architecture. Instead, we found that five aggregates (all but B_{28%}) shared similar responses to freeze–thaw in pore coordination number frequency and pore throat diameter distribution, whereas B_{28%} consistently showed a divergent response. The inconsistent response to freeze–thaw by pore networks comprising platy pores intersecting tubular pores necessitates expanded testing to identify if response variability is a widespread trend amongst that particular pore morphology. The common changes we observed across pore networks with contrasting pore morphologies—pore coordination number frequency increasing for less connected pores and pore throat diameter distributions showing increased response to freeze–thaw in the 30–50- μm range—should also be investigated for wider trends in aggregate response to freeze–thaw.

The decreasing volumes observed in connected water-filled pores do not correspond with an increase in any other volumetric fraction (Fig. 4), raising questions of what freezing-associated intra-aggregate mechanisms or method artifacts may be causing these decreases. We speculate that the increase in air-filled pores for A_{28%} is indeed an artifact of different regions sampled for the post-freeze–thaw scan and the pre-freeze–thaw scan (this was the only aggregate in which different regions were scanned). While the volumetric fraction of connected water-filled pores was reduced following freeze–thaw, there was not a significant decrease in total connected pore volume. Rather, there is a shift toward fewer pore connections reflected in the lower pore coordination number following freeze–thaw (Fig. 5). The decrease in well-connected pores (directly connected to eight or more other pores) and

increase in singly connected pores indicates that while connectivity may not be decreasing within the first five freeze–thaw cycles, the pore network is becoming more vulnerable to future responses of pores and pore throats to deformation that could result in decreased connectivity and isolation of portions of the pore network. Previous findings by Ma et al. (2021) linked freeze–thaw to increased pore connectivity, a significant finding in the context of previous studies that emphasize the importance of network connectivity in oxygen availability, water transport, and nutrient diffusion (Wanzek et al., 2018). However, findings from Ma et al. (2021) specified increasing porosity following seven freeze–thaw cycles (and up to 20 freeze–thaw cycles), with pore connectivity showing unpredictable response up through the first seven freeze–thaw cycles. The inconsistent response of connected pore volumes to freeze–thaw observed in our experiment aligns with these findings and suggests a potential difficulty in predicting pore connectivity and thus redox chemistry and nutrient diffusion in the incipient stages of freeze–thaw following permafrost thaw. Ma et al. (2021) also observed decreases in the total number of pores following multiple freeze–thaw cycles. We found no statistical change in the number of pore throats following freeze–thaw, likely due to the high variability in pore throat counts across the replicates (ranging from 23 to 552). However, five out of six aggregates ($A_{28\%}$ excluded) did show decreased pore throat counts following freeze–thaw (ST3), aligning with Ma et al. (2021).

The decrease in the number of connected pore throats following freeze–thaw contrasts findings from Liu et al. (2021b) where an increase in the number of pores in aggregates occurred following freeze–thaw cycling (resolution $> 25 \mu\text{m}$). One possible explanation for the differences observed between the two studies may relate to non-complementary experimental designs. Liu et al. (2021b) studied freeze–thaw response in soil columns whereas our work focused on soil aggregates. The impact of freeze–thaw on a soil column is influenced by the constraints of the core jacket and by the uniform dimensions provided by the core. The irregular and less constrained shapes of the aggregates (like those used within our study) may provide uneven stress to the samples during freezing, encouraging expansion toward regions of the aggregate not constrained by the sample holder while a fully contained core will likely undergo evenly distributed stress throughout. These differences in constraint and subsequent impacts to expansion during freezing could affect pore and pore throat deformation, although in reviewing the literature we were unable to find any studies that quantify the impact of structural constraints on expansion in aggregates and cores during freezing.

The increasing frequency of singly connected pores (pore coordination number 1) could be the result of either expansion or contraction resulting from freeze–thaw deformation. Smaller pores and pore throats ($< 20 \mu\text{m}$) may be undergoing expansion following freeze–thaw (Chamberlain et al., 1990), enabling their detection at our 20- μm analysis resolution and thus contributing to the increased frequency in lower pore coordination numbers post-freeze–thaw. However, more well-connected pores could be undergoing throat contraction or collapse, resulting in increased frequencies of smaller pore throats. We also observed decreases in the total number of pore throats in most aggregates following freeze–thaw. A decrease in pore throat counts contradicts the suggestion that there is an influx of smaller pore throats that are expanding into resolution and provides support for contraction causing the increased frequency in smaller pore throat diameters (ST3). The potential for deformation highlights the importance of examining freeze–thaw response of the structure and size of micropores ($< 25 \mu\text{m}$) due to the pivotal role they play in microbial activity and organic matter decomposition (Ruamps et al., 2011; Waring et al., 2020).

4.3. Pore throat diameter

Overall, we did not find evidence of uniform expansion or uniform collapse within certain pore throat diameter ranges. The occurrence of

peaks splitting (a pre-freeze–thaw peak splitting into two smaller peaks that are positioned to each side of the original peak) is widespread across the pore throat diameter distributions of all aggregates (Fig. 6) indicating that crystallization pressure acting on diameters of 30–40 μm may result in both collapsing and expanding pore throats. This lack of cohesive trend in pore throat size supports previous observations of fluctuating pore size in freeze–thaw incubations with less than seven freeze–thaw cycles (Ma et al., 2021). Combined expansion of some and collapse of other pore throats may be driven by fluid pressure gradients across the soil pore network controlled by both temperature gradients (Rempel, 2010; Wetzlaufer et al., 1996; Wilen and Dash, 1995) and by crystallization pressures across different pore sizes, which would result in a variable combination of both expansion and contraction throughout pore throats of different sizes. This network approach complicates current interpretations of freeze–thaw data that suggest deformation type is dependent on pore size (Chamberlain and Gow, 1979; Starkloff et al., 2017). Ma et al. (2021) identified a general shift in pore size dimensions following (but not prior to) seven freeze–thaw cycles, suggesting that deformation resilience (or recovery following crystal deformation) may weaken as soil aggregates undergo more freeze–thaw cycles. Following 20 freeze–thaw cycles, Ma et al. (2021) found an overall increase in pore size and thus air infiltration rates. The potential to increase overall pore connectivity beyond the first stages of freeze–thaw encourages further investigation as increases in pore and pore throat size as well as changing connectivity could impact gas release from thawing permafrost through increased substrate-microbe interactions and availability of previously isolated substrates (Ananyeva et al., 2013; Bailey et al., 2017; Strong et al., 2004; Wanzek et al., 2018; Waring et al., 2020).

Based on the changes we identified in pore throat size and pore connectivity—which provide evidence that deformation is occurring within pore throats following freeze–thaw—and the findings of Ma et al. (2021) regarding changes to pore shape factor, we anticipated pore throat deformation being visible in either increasing sphericity or elongation of pore throats. We interpret the lack of change in pore shape factor within the most impacted pore throat sizes to indicate that pore network response to freeze–thaw resulting in clear elongation or spheicity of pore throats is not yet evident during the incipient stage of deformation. Despite less deformation than may be observed in further freeze–thaw cycles, the incipient stage does show evidence for changing pore network connectivity and pore throat size distribution.

4.4. Conclusions

Freeze–thaw impacts to the pore network occur within the first five freeze–thaw cycles and may be dependent on initial pore morphology. Changes in connectivity following freeze–thaw were complex, with overall connected pore volume showing no response to freeze–thaw while shifts in individual pore connectedness and pore throat size distribution provided evidence for widespread contraction of pore throats. Our findings indicate that this early deformation could lower the resiliency of the pore network to future freeze–thaw deformation by decreasing pore connections and subsequently increasing vulnerability of the pore network to disconnection. The incipient stage of deformation encompasses the freeze–thaw cycles following initial permafrost thaw, co-occurring with heightened microbial activity and organic matter decomposition due to warming (Cavicchioli et al., 2019; Liu et al., 2020). Predicting biogeochemical function and transformation following thaw requires understanding how soil properties, which control those functions, also shift following repeated freeze–thaw.

The role that pore morphology plays in the magnitude and outcome of freeze–thaw response warrants further investigation, as deformation during freeze–thaw may be linked to that initial pore structure. This is especially pertinent in permafrost soils characterized by distinct pore structures associated with cryogenic processes (Ping et al., 2015). We posit that aggregates containing platy-pore structures intersecting channel pores may respond to freeze–thaw with greater variability than

aggregates with more homogenous pore morphologies. Future work should also aim to untangle how initial saturation levels and freezing rates may contribute to variability of freeze-thaw response by the soil pore network.

Impacts of freeze-thaw at the micro-scale are responsible for ecologically important soil processes, such as water holding capacity and microbial access to and subsequent decomposition of carbon compounds (Wanzek et al., 2018; Waring et al., 2020). As the Arctic continues to change under warming conditions, our ability to understand the guiding processes of permafrost landscape transition relies upon an enhanced knowledge of how freeze-thaw will affect soil properties at the micro- and macro-scale. Examining the response of soil physical properties to freeze-thaw is vital to predicting the behavior of future permafrost landscapes.

5. Data availability

All data and scripts are available at <https://github.com/Erin-Rooney/XCT-freezethaw> (<https://doi.org/10.5281/zenodo.5816355>) and archived and searchable at <https://search.emsl.pnnl.gov/>.

Declaration of Competing Interest

The authors declare that they have no known competing financial interests or personal relationships that could have appeared to influence the work reported in this paper.

Acknowledgments

This research was supported by the U.S. Department of Energy, Office of Science, Biological and Environmental Research as part of the Environmental System Science Program. The Pacific Northwest National Laboratory is operated for DOE by Battelle Memorial Institute under contract DE-AC05-76RL01830. A portion of this research was performed on a project award no. 50267 from the Environmental Molecular Sciences Laboratory (grid.436923.9), a DOE Office of Science user facility sponsored by the Department of Energy's Office of Biological and Environmental Research program under Contract No. DE-AC05-76RL01830 and located at Pacific Northwest National Laboratory. NEON is sponsored by the National Science Foundation (NSF) and operated under cooperative agreement by Battelle. This material is based in part upon work supported by NSF through the NEON program.

Appendix A. Supplementary data

Supplementary data to this article can be found online at <https://doi.org/10.1016/j.geoderma.2021.115674>.

References

- Ananyeva, K., Wang, W., Smucker, A.J.M., Rivers, M.L., Kravchenko, A.N., 2013. Can intra-aggregate pore structures affect the aggregate's effectiveness in protecting carbon? *Soil Biol. Biochem.* 57, 868–875. <https://doi.org/10.1016/j.soilbio.2012.10.019>.
- Andersland, O.B., Ladanyi, B., 2004. *Frozen Ground Engineering*, second ed. John Wiley & Sons.
- Bailey, V.L., Fansler, S.J., Stegen, J.C., McCue, L.A., 2013. Linking microbial community structure to β-glucosidase function in soil aggregates. *ISME J.* 7 <https://doi.org/10.1038/ismej.2013.87>.
- Bailey, V.L., Smith, A.P., Tfaily, M., Fansler, S.J., Bond-Lamberty, B., 2017. Differences in soluble organic carbon chemistry in pore waters sampled from different pore size domains. *Soil Biol. Biochem.* 107, 133–143. <https://doi.org/10.1016/j.soilbio.2016.11.025>.
- Biskaborn, B.K., Smith, S.L., Noetzli, J., Matthes, H., Vieira, G., Streletskiy, D.A., Schoeneich, P., Romanovsky, V.E., Lewkowicz, A.G., Abramov, A., Allard, M., Boike, J., Cable, W.L., Christiansen, H.H., Delaloye, R., Diekmann, B., Drozdov, D., Etzelmüller, B., Grosse, G., Guglielmin, M., Ingeman-Nielsen, T., Isaksen, K., Ishikawa, M., Johansson, M., Johannsson, H., Joo, A., Kaverin, D., Khodolov, A., Konstantinov, P., Kröger, T., Lambiel, C., Lanckman, J.P., Luo, D., Malkova, G., Meiklejohn, I., Moskalenko, N., Oliva, M., Phillips, M., Ramos, M., Sammel, A.B.K., Sergeev, D., Seybold, C., Skryabin, P., Vasiliiev, A., Wu, Q., Yoshikawa, K., Zheleznyak, M., Lantuit, H., 2019. Permafrost is warming at a global scale. *Nat. Commun.* 10 <https://doi.org/10.1038/s41467-018-08240-4>.
- Blackwell, M.S.A., Brookes, P.C., de la Fuente-Martinez, N., Gordon, H., Murray, P.J., Snars, K.E., Williams, J.K., Bol, R., Haygarth, P.M., 2010. Phosphorus solubilization and potential transfer to surface waters from the soil microbial biomass following drying-rewetting and freezing-thawing. In: *Advances in Agronomy*. Academic Press Inc., pp. 1–35. [https://doi.org/10.1016/S0065-2113\(10\)06001-3](https://doi.org/10.1016/S0065-2113(10)06001-3).
- Boswell, E.P., Balster, N.J., Bajcz, A.W., Thompson, A.M., 2020a. Soil aggregation returns to a set point despite seasonal response to snow manipulation. *Geoderma* 357. <https://doi.org/10.1016/j.geoderma.2019.113954>.
- Boswell, E.P., Thompson, A.M., Balster, N.J., Bajcz, A.W., 2020b. Novel determination of effective freeze-thaw cycles as drivers of ecosystem change. *J. Environ. Qual.* 49, 314–323. <https://doi.org/10.1002/jeq2.20053>.
- Brown, J., Romanovsky, V.E., 2008. Report from the International Permafrost Association: State of permafrost in the first decade of the 21st century. *Permafrost Periglac. Process.* 255–260. <https://doi.org/10.1002/PPP.618>.
- Cavicchioli, R., Ripple, W.J., Timmis, K.N., Azam, F., Bakken, L.R., Baylis, M., Behrenfeld, M.J., Boetius, A., Boyd, P.W., Classen, A.T., Crowther, T.W., Danovaro, R., Foreman, C.M., Huismann, J., Hutchins, D.A., Jansson, J.K., Karl, D.M., Koskiela, B., Mark Welch, D.B., Martiny, J.B.H., Moran, M.A., Orphan, V.J., Reay, D.S., Remais, J.V., Rich, V.I., Singh, B.K., Stein, L.Y., Stewart, F.J., Sullivan, M.B., van Oppen, M.J.H., Weaver, S.C., Webb, E.A., Webster, N.S., 2019. Scientists' warning to humanity: microorganisms and climate change. *Nat. Rev. Microbiol.* 17 <https://doi.org/10.1038/s41579-019-0222-5>.
- Chadburn, S.E., Burke, E.J., Cox, P.M., Friedlingstein, P., Hugelius, G., Westermann, S., 2017. An observation-based constraint on permafrost loss as a function of global warming. *Nat. Clim. Change* 7, 340–344. <https://doi.org/10.1038/nclimate3262>.
- Chamberlain, E.J., Iskveer, I., and Hunziker, S.E. (1990) Effect of Freeze-Thaw on the Permeability and Macrostructure of Soils. Proceedings International Symposium on Frozen Soil Impacts on Agricultural, Range, and Forest Lands, Spokane, 21–22 March 1990, 145–155.
- Chamberlain, E.J., Gow, A.J., 1979. Effect of freezing and thawing on the permeability and structure of soils. *Eng. Geol.* 13, 73–92.
- Darrow, M.M., Lieblappen, R.M., 2020. Visualizing cation treatment effects on frozen clay soils through µCT scanning. *Cold Reg. Sci. Technol.* 175 <https://doi.org/10.1016/j.coldregions.2020.103085>.
- DeMarco, J., Mack, M.C., Bret-Harte, M.S., 2011. The effects of snow, soil microenvironment, and soil organic matter quality on N availability in Three Alaskan Arctic Plant Communities. *Ecosystems* 14. <https://doi.org/10.1007/s10021-011-9447-5>.
- Deprez, M., de Kock, T., de Schutter, G., Cnudde, V., 2020. The role of ink-bottle pores in freeze-thaw damage of oolithic limestone. *Constr. Build. Mater.* 246 <https://doi.org/10.1016/j.conbuildmat.2020.118515>.
- Ferreira, T.R., Pires, L.F., Wildenschmid, D., Heck, R.J., Antonino, A.C.D., 2018. X-ray microtomography analysis of lime application effects on soil porous system. *Geoderma* 324, 119–130. <https://doi.org/10.1016/j.geoderma.2018.03.015>.
- Freppaz, M., Viglietti, D., Balestrini, R., Lonati, M., Colombo, N., 2019. Climatic and pedoclimatic factors driving C and N dynamics in soil and surface water in the alpine tundra (NW-Italian Alps). *Nature Conserv. 34* <https://doi.org/10.3897/natureconservation.34.30737>.
- Gao, Z., Hu, X., Li, X.-Y., Li, Z.-C., 2021. Effects of freeze-thaw cycles on soil macropores and its implications on formation of hummocks in alpine meadows in the Qinghai Lake watershed, northeastern Qinghai-Tibet Plateau. *J. Soils Sediments* 21. <https://doi.org/10.1007/s11368-020-02765-2>.
- Gao, D., Zhang, L., Liu, J., Peng, B., Fan, Z., Dai, W., Jiang, P., Bai, E., 2018. Responses of terrestrial nitrogen pools and dynamics to different patterns of freeze-thaw cycle: a meta-analysis. *Glob. Change Biol.* 24, 2377–2389. <https://doi.org/10.1111/gcb.14010>.
- Henry, H.A.L., 2008. Climate change and soil freezing dynamics: Historical trends and projected changes. *Clim. Change* 87, 421–434. <https://doi.org/10.1007/s10584-007-9322-8>.
- Jelinski, N.A., Sousa, M.J., Williams, A., GreyBear, E., Finnesand, K., Mulligan, D., Cole, C., Stillinger, M.D., Feinberg, J.M., 2019. Cryoturbation and Carbon Stocks in Gelisols under late-successional black spruce forests of the Copper River Basin, Alaska. *Soil Sci. Soc. Am. J.* 83 <https://doi.org/10.2136/sssaj2019.07.0212>.
- Lawlor, J., 2020. PNWColors: Color Palettes Inspired by Nature in the US Pacific Northwest. Zenodo.
- Li, X., Lu, Y., Zhang, X., Fan, W., Lu, Y., Pan, W., 2019. Quantification of macropores of Malan loess and the hydraulic significance on slope stability by X-ray computed tomography. *Environ. Earth Sci.* 78 <https://doi.org/10.1007/s12665-019-8527-2>.
- Liu, B., Fan, H., Han, W., Zhu, L., Zhao, X., Zhang, Y., Ma, R., 2021a. Linking soil water retention capacity to pore structure characteristics based on X-ray computed tomography: Chinese Mollisol under freeze-thaw effect. *Geoderma* 401. <https://doi.org/10.1016/j.geoderma.2021.115170>.
- Liu, M., Feng, F., Cai, T., Tang, S., 2020. Soil Microbial Community Response Differently to the Frequency and Strength of Freeze-Thaw Events in a Larix gmelinii Forest in the Daxing'an Mountains, China. *Front. Microbiol.* 11 <https://doi.org/10.3389/fmicb.2020.01164>.
- Liu, B., Ma, R., Fan, H., 2021b. Evaluation of the impact of freeze-thaw cycles on pore structure characteristics of black soil using X-ray computed tomography. *Soil Tillage Res.* 206 <https://doi.org/10.1016/j.still.2020.104810>.
- Ma, R., Jiang, Y., Liu, B., Fan, H., 2021. Effects of pore structure characterized by synchrotron-based micro-computed tomography on aggregate stability of black soil under freeze-thaw cycles. *Soil Tillage Res.* 207 <https://doi.org/10.1016/j.still.2020.104855>.
- Mackay, J.R., 1980. The origin of hummocks, western Arctic coast, Canada. *J. Earth Sci.*

- Nave, L.E., Heckman, K.A., Bowman, M., Gallo, A.C., Hatten, J., Matosziuk, L., Possinger, A., SanClements, M., Strahm, B., Weiglein, T.L., Swanston, C., 2021. Soil Organic Matter Mechanisms of Stabilization (SOMMOS) - enhanced soil characterization data from 40 National Ecological Observatory Network (NEON) sites ver 1. Environmental Data Initiative. <https://doi.org/10.6073/pasta/99d113534ecaa04e820850e6169be04d> (Accessed 2021-10-26).
- NEON (National Ecological Observatory Network), 2019. Terrestrial Observation System (TOS) Site Characterization Report: Domain 18.
- NEON (National Ecological Observatory Network). RELEASE-2021 (DP1.00041.001). Dataset accessed from <https://data.neonscience.org> on June 29, 2021.
- NEON (National Ecological Observatory Network). Bundled data products - eddy covariance, RELEASE-2021 (DP4.00200.001). Dataset accessed from <https://data.neonscience.org> on June 29, 2021.
- NEON (National Ecological Observatory Network). Soil physical and chemical properties, Megapit, RELEASE-2021 (DP1.00096.001). Dataset accessed from <https://data.neonscience.org> on June 29, 2021.
- Nimmo, J.R., 2013. Porosity and Pore Size Distribution, in: Reference Module in Earth Systems and Environmental Sciences. Elsevier. doi:10.1016/B978-0-12-409548-9.05265-9.
- Ping, C.L., Michaelson, G.J., Kimble, J.M., Romanovsky, V.E., Shur, Y.L., Swanson, D.K., Walker, D.A., 2008. Cryogenesis and soil formation along a bioclimate gradient in Arctic North America. *J. Geophys. Res. Biogeosci.* 113 <https://doi.org/10.1029/2008JG000744>.
- Ping, C.L., Jastrow, J.D., Jorgenson, M.T., Michaelson, G.J., Shur, Y.L., 2015. Permafrost soils and carbon cycling. *SOIL* 1, 147–171. <https://doi.org/10.5194/soil-1-147-2015>.
- R Core Team, 2020. R: A language and environment for statistical computing.
- Rempel, A.W., van Alst, L.J., 2013. Potential gradients produced by pore-space heterogeneities: Application to isothermal frost damage and submarine hydrate anomalies.
- Rempel, A.W., 2010. Frost heave.
- Ruamps, L.S., Nunan, N., Chen, C., 2011. Microbial biogeography at the soil pore scale. *Soil Biol. Biochem.* 43 <https://doi.org/10.1016/j.soilbio.2010.10.010>.
- Schuur, E.A.G., McGuire, A.D., Schädel, C., Grosse, G., Harden, J.W., Hayes, D.J., Hugelius, G., Koven, C.D., Kuhry, P., Lawrence, D.M., Natali, S.M., Olefeldt, D., Romanovsky, V.E., Schaefer, K., Turetsky, M.R., Treat, C.C., Vonk, J.E., 2015. Climate change and the permafrost carbon feedback. *Nature*. <https://doi.org/10.1038/nature14338>.
- Soil Survey Staff, 1999. Soil taxonomy: A basic system of soil classification for making and interpreting soil surveys, 2nd edition. ed. Natural Resources Conservation Service, U.S. Department of Agriculture Handbook 436.
- Soil Survey Staff, 2014. Keys to Soil Taxonomy, 12th ed. USDA-Natural Resources Conservation Service, Washington, DC.
- Song, Y., Zou, Y., Wang, G., Yu, X., 2017. Altered soil carbon and nitrogen cycles due to the freeze-thaw effect: a meta-analysis. *Soil Biol. Biochem.* 109, 35–49. <https://doi.org/10.1016/j.soilbio.2017.01.020>.
- Soulides, D.A., Allison, F.E., 1961. Effect of drying and freezing soils on carbon dioxide production, available mineral nutrients, aggregation, and bacterial population. *Soil Sci.* 91 <https://doi.org/10.1097/00010694-196105000-00001>.
- Starkloff, T., Larsbo, M., Stolte, J., Hessel, R., Ritsema, C., 2017. Quantifying the impact of a succession of freezing-thawing cycles on the pore network of a silty clay loam and a loamy sand topsoil using X-ray tomography. *Catena* 156, 365–374. <https://doi.org/10.1016/j.catena.2017.04.026>.
- Storey, K.B., Storey, J.M., 2005. FREEZE TOLERANCE.
- Strong, D.T., de Wever, H., Merckx, R., Recous, S., 2004. Spatial location of carbon decomposition in the soil pore system. *Eur. J. Soil Sci.* 55, 739–750. <https://doi.org/10.1111/j.1365-2389.2004.00639.x>.
- U.S. Geological Survey, 2005. Mineral Resources Data System: U.S. Geological Survey, Reston, Virginia.
- Veelen, A., Koebernick, N., Scotson, C.S., McKay-Fletcher, D., Huthwelker, T., Borca, C.N., Mosselmans, J.F.W., Roose, T., 2020. Root-induced soil deformation influences Fe, S and P: rhizosphere chemistry investigated using synchrotron XRF and XANES. *New Phytol.* 225 <https://doi.org/10.1111/nph.16242>.
- Wadell, H., 1933. Sphericity and Roundness of Rock Particles. *J. Geol.* 41.
- Wang, T., Hamann, A., Spittlehouse, D.L., Murdoch, T.Q., 2012. ClimateWNA—high-resolution spatial climate data for Western North America. *J. Appl. Meteorol. Climatol.* 51 <https://doi.org/10.1175/JAMC-D-11-043.1>.
- Wanzek, T., Keiluweit, M., Varga, T., Lindsley, A., Nico, P.S., Fendorf, S., Kleber, M., 2018. The ability of soil pore network metrics to predict redox dynamics is scale dependent. *Soil Syst.* 2 <https://doi.org/10.3390/soilsystems2040066>.
- Waring, B.G., Sulman, B.N., Reed, S., Smith, A.P., Averill, C., Creamer, C.A., Cusack, D.F., Hall, S.J., Jastrow, J.D., Jilling, A., Kemner, K.M., Kleber, M., Liu, X.A., Pett-Ridge, J., Schulz, M., 2020. From pools to flow: The PROMISE framework for new insights on soil carbon cycling in a changing world. *Glob. Change Biol.* 26 <https://doi.org/10.1111/gcb.15365>.
- Wei, C., Yu, S., Jichun, W., Yaling, C., Erxing, P., Leonid, G., 2021. Soil hydrological process and migration mode influenced by the freeze-thaw process in the activity layer of permafrost regions in Qinghai-Tibet Plateau. *Cold Regions Sci. Technol.* 184 <https://doi.org/10.1016/j.coldregions.2021.103236>.
- Wettlaufer, J.S., Worster, M.G., Wilen, L.A., Dash, J.G., 1996. A Theory of Premelting Dynamics for all Power Law Forces.
- Wickham, H., 2016. *ggplot2: Elegant Graphics for Data Analysis*. Springer.
- Wickham, H., François, R., Henry, L., 2020. dplyr: A grammar of Data Manipulation.
- Wilen, L.A., Dash, J.G., 1995. Frost Heave Dynamics.
- Zhao, Y., Hu, X., Li, X., Jiang, L., Gao, Z., 2021a. Evaluation of the impact of freeze-thaw cycles on the soil pore structure of alpine meadows using X-ray computed tomography. *Soil Sci. Soc. Am. J.* <https://doi.org/10.1002/saj2.20256>.
- Zhao, Y., Li, Y., Yang, F., 2021b. Critical review on soil phosphorus migration and transformation under freezing-thawing cycles and typical regulatory measurements. *Sci. Total Environ.* 751 <https://doi.org/10.1016/j.scitotenv.2020.141614>.